Overview of research and recent results using receiver functions

ADVANCED STUDIES COURSE IN JOINT INVERSION OF RECEIVER FUNCTIONS AND SURFACE WAVE DISPERSION
Kuwait City, KUWAIT
19 January, 2013

Michael E. Pasyanos
Lawrence Livermore National Laboratory

LLNL-PRES-609979

Lawrence Livermore National Laboratory, P. O. Box 808, Livermore, CA 94551

This work performed under the auspices of the U.S. Department of Energy by Lawrence Livermore National Laboratory under Contract DE-AC52-07NA27344

Classic Receiver Function Papers

Papers that describe the basic functionality of teleseismic receiver function analysis

- Langston (1979) – Deconvolution procedure - 608 citations in Web of Science (1/2013)
- Owens et al. (1984) – RF stacking - 230 citations
- Ammon et al. (1990) – Non-uniqueness of RFs - 285 citations
- Ammon (1991) – Importance of absolute amplitudes - 265 citations
- Ligorría and Ammon (1999) – Iterative deconvolution – 207 citations


VOL. 84, NO. B9 JOURNAL OF GEOPHYSICAL RESEARCH AUGUST 10, 1979

Structure Under Mount Rainier, Washington, Inferred From Teleseismic Body Waves

CHARLES A. LANGSTON

Department of Geosciences, Pennsylvania State University, University Park, Pennsylvania 16802

Teleseismic long-period *P* waves recorded at the World-Wide Standard Seismograph Network station LON (Longmire, Washington) are shown to exhibit strong anomalous particle motion not attributable to instrument miscalibration or malfunction. In particular, a large and azimuthally smoothly varying tangential component is observed after vector rotation of horizontal *P* waves into the ray direction and after application of a deconvolution technique which equalizes effective source time functions and removes the instrument response. These tangential waves attain amplitudes comparable to the radial component and demonstrate wave form antisymmetry about a NNE azimuth. A model which contains a single high-contrast interface dipping toward the NNE at a depth of 15–20 km can explain most of the characteristics of the long-period *P* wave data, provided dips are greater than about 10° and only the interference of *P* and *Ps* generated at the interface is considered. The model breaks down for later arrivals which are presumably multiples or scattered waves. Examination of long-period *S* waves from several deep teleseisms shows a prominent *Sp* arrival 18 s before *S*. The timing of this phase conversion suggests an interface at about 145-km depth, and its sense of polarity suggests that the velocity contrast is from higher to lower velocities as depth decreases. This interface may correspond to the bottom of the upper mantle low-velocity zone in the area.

INTRODUCTION

From a geologist's point of view, the top of the earth's crust is composed of a myriad of differing rock types with readily discernable lateral variations in lithologies and structures. On the basis of these surface observations it is easy and probably justified to assume that the entire crustal and upper mantle column behaves in a similar complicated way. Recent high-resolution reflection profiling and other seismological studies are beginning to support this view [e.g., *Smithson,* 1978; *Aki et al.,* 1977]. However, when seismic waves are used to deduce earth structure, the usual state of affairs is to assume vertically inhomogeneous earth models with no lateral variations. This assumption is good in many cases because, to first order, the earth appears to be radially stratified and seismic waves fortunately average over distance scales comparable to their wavelength.

This paper examines an interesting case where the seismic data cannot be explained with any vertically inhomogeneous nonlaterally varying earth model. Teleseismic *P* and *S* waves as recorded at the World-Wide Standard Seismograph Network (WWSSN) station LON (Longmire, Washington) were examined to determine crustal and upper mantle structure beneath the station. A previous study of teleseismic body waves at COR (Corvallis, Oregon) and of *P* wave forms recorded teleseismically from the 1965 Puget Sound earthquake indicated that the area of western Washington and Oregon might be underlain by a distinct low-velocity zone (LVZ) [*Langston,* 1977*a*; *Langston and Blum,* 1977]. The base of this LVZ was inferred to be at 55-km depth under Puget Sound and at 45-km depth under COR. LON, which is located on the flank of Mount Rainier, a Quaternary stratovolcano, was chosen for study in an attempt to define the limits of this LVZ.

It was immediately apparent upon examination and comparison of the long-period *P* wave form data that earth structure at LON is radically different from structure under COR. As is the usual case when new data are considered, new questions and problems immediately arose with respect to both the regional structure picture and seismic wave propagation. The most dramatic aspect of the data from LON is that long-period *P* waves exhibited a large tangential component of ground motion. The simple existence of 'tangential *P* waves' automatically precludes any explanation or interpretations using honogeneous plane layered earth models, since the *P-SV* and *SH* wave systems are decoupled.

The study of these waves will be based on a timid extension of standard seismological practice. Using theory presented in a previous paper [*Langston,* 1977*b*], earth models will still have planar interfaces, but these interfaces will be allowed to dip. A three-dimensional ray-tracing formalism is used to find the path of rays in the structure. Ray amplitudes are computed by first decomposing the incident ray into *P-SV* and *SH* components in local interface coordinates, multiplying each amplitude by the appropriate plane wave reflection or transmission coefficient, and then propagating the wave to the next interface, where the procedure is repeated. Diffracted waves from structure edges or corners are not included. Hence all 'tangential *P*' wave effects will be explained by off-azimuth arrivals of primary, converted, and reverberated rays. This is a hypothesis which was only partially successful in explaining the observed *P* wave data, whether because of a breakdown in theory (existence of diffracted waves) or in assuming planar interfaces (other geometries or topography).

After a short description of regional tectonics and setting, this study will be presented in four parts. First, the long-period *P* wave form data recorded at LON will be presented with a discussion of instrument calibration. This is crucial, since instrument miscalibration or malfunction is the first likely cause of apparent tangential *P* waves. Next, a general method for equalizing the wave form data for arbitrary effective source time function will be discussed. Afterward, the equalized *P* wave form data will be interpreted by calculating theoretical ray amplitudes and synthetic seismograms from earth models with planar dipping interfaces. The final section presents results concerning long-period *S* wave form data. While not adding significant constraints to earth models deduced from the *P* wave data, there is an indication of an interface at approximately 145-km depth under LON from *Sp* precursor observations.

Paper number 9B0335.
0148-0227/79/009B-0335$01.00

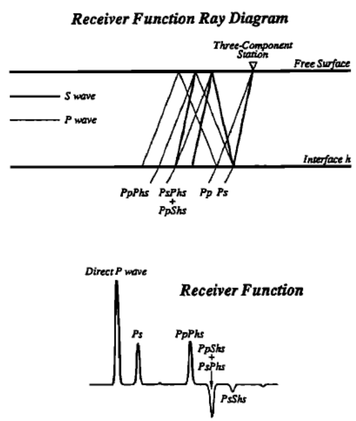

Fig. 1. (Top) Simplified ray diagram identifying the major *P*-to-*S* converted phases which comprise the receiver function for a single layer over a half-space. (Bottom) The waveform corresponding to the model presented above.

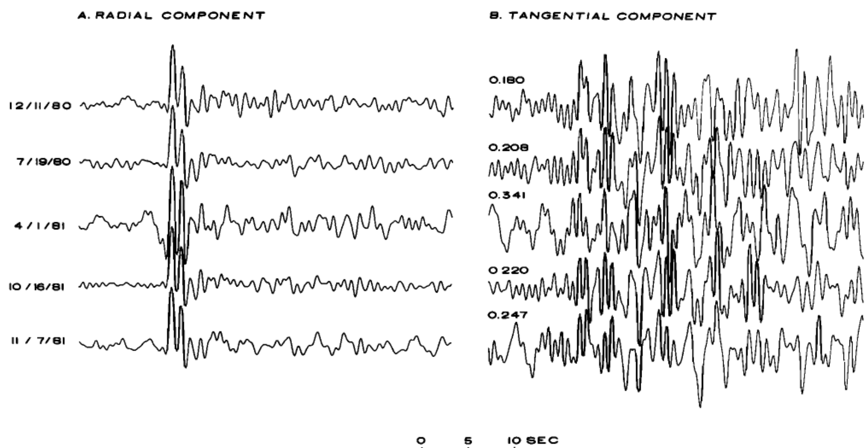

Fig. 4. Stacking suite for RSCP SE back azimuth: (*a*) radial component (positive away from the arriving event) and (*b*) tangential component (positive clockwise from positive radial direction). The tangential/radial amplitude ratio is shown at the start of each tangential trace.

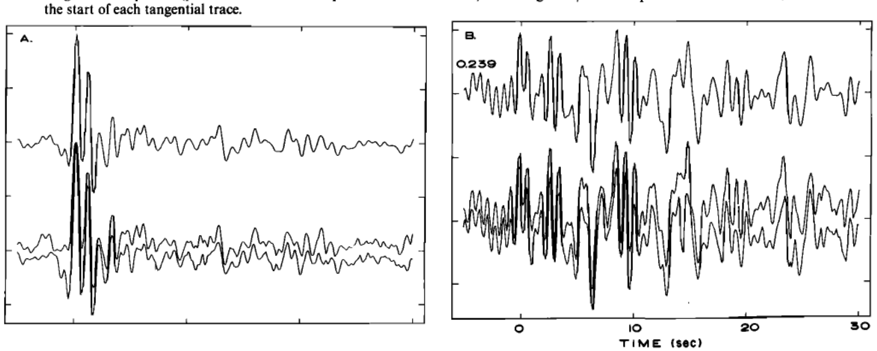

Overview of recent receiver function papers focused on the Middle East (with emphasis on Arabia and Anatolia)

- Sandvol et al. (1998a) – RFs, Arabia
- Sandvol et al. (1998b) – RFs, Middle East and North Africa
- Mangino and Priestley (1998) – RFs, southern Caspian
- Julià et al. (2000) - Joint inversion of RFs and SWs, method
- Julià et al. (2003) – Joint inversion of RFs and SWs, western Arabia
- Zor et al. (2003) – RFs, eastern Turkey
- Rodgers et al. (2003) – RFs, Jordan
- Moshen et al. (2005) – RFs, Dead Sea Fault
- Al-Damegh et al. (2005) – RFs, Arabia
- Tkalčić et al. (2006) – Joint inversion of RFs and SWs, Arabia
- Paul et al. (2006) - RFs, stacking, gravity modeling, Zagros Mts
- Angus et al. (2006) – S-wave receiver functions, eastern Turkey
- Pasyanos et al. (2007) – Joint inversion of RFs and SWs, travel times, Kuwait
- Gök et al. (2007) – Joint inversion of RFs and SWs, eastern Turkey
- Gök et al. (2007) – Joint inversion of RFs and SWs, Iraq
- Hansen et al. (2007) – S-wave receiver functions, Arabia
- Al-Hashmi (2011) – Joint inversion of RFs and SWs, Oman
- Gök et al. (2011) – Joint inversion of RFs and SWs, eastern Turkey and Caucasus
- Gök (in preparation) – Joint inversion of RFs and SWs, Mesopotamian Foredeep

Receiver functions for the Middle East and North Africa

Sandvol et al. (1998) JGR

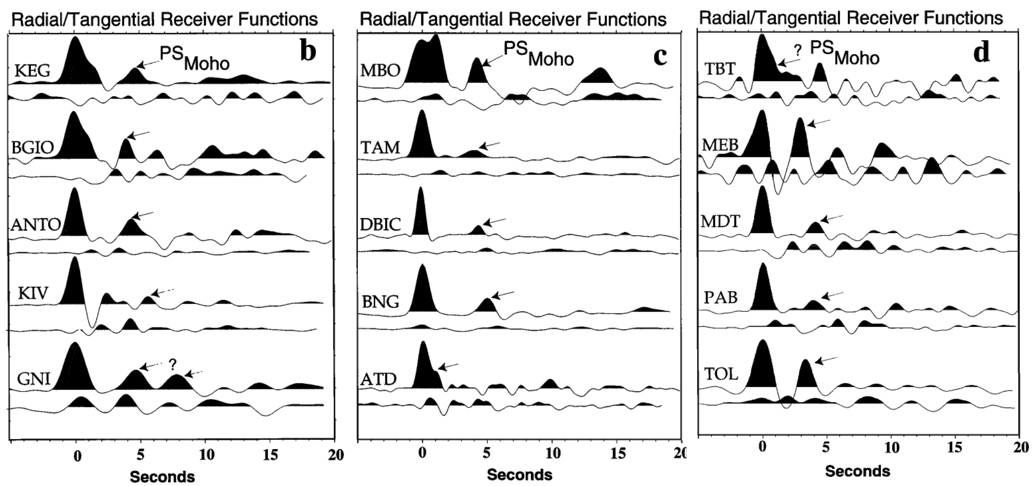

RFs for separated stations in the Middle East and North Africa

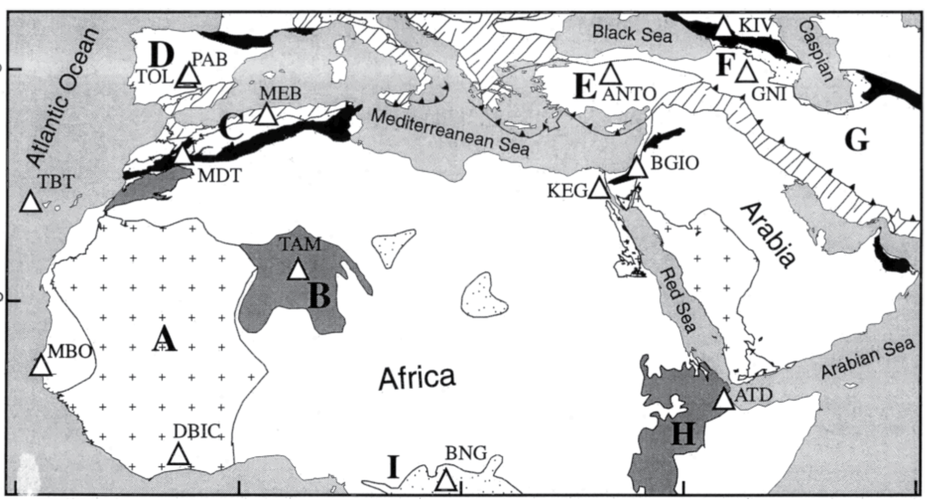

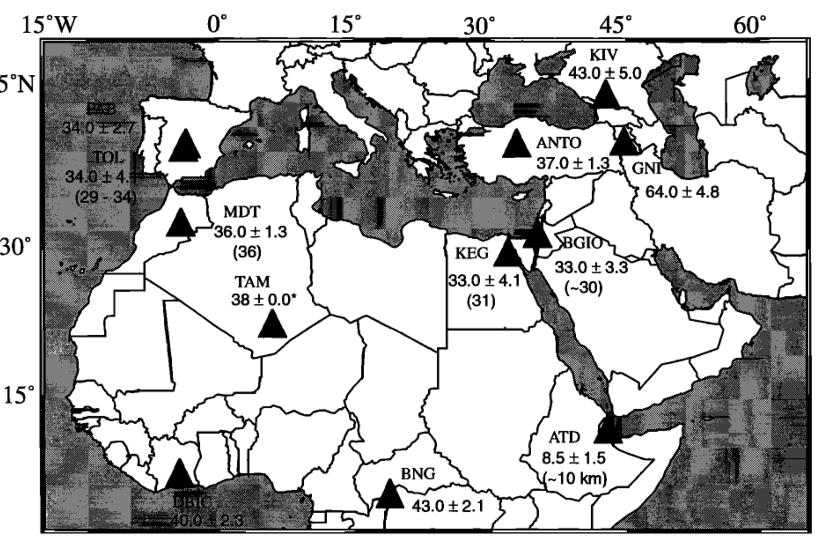

Figure 14. A map showing the grid search results of crustal thickness and prior, if available, estimates of crustal thickness (shown in parentheses), and jackknife error estimates in the Middle East and Africa.

Receiver functions for the Arabian Peninsula

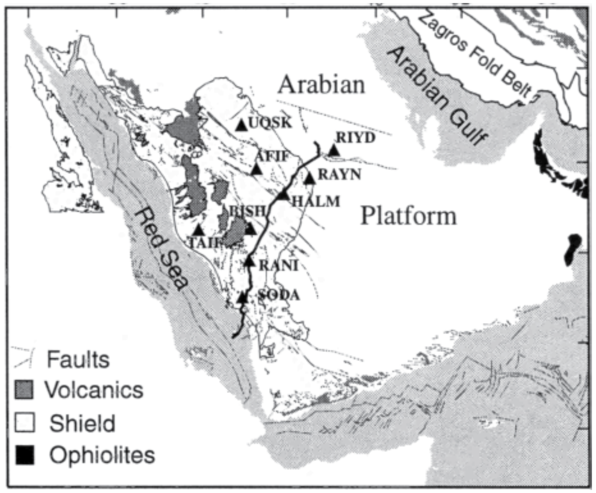

Sandvol et al. (1998) GRL

Saudi PASSCAL deployment

Studying stations in close proximity can yield insights on tectonic structure

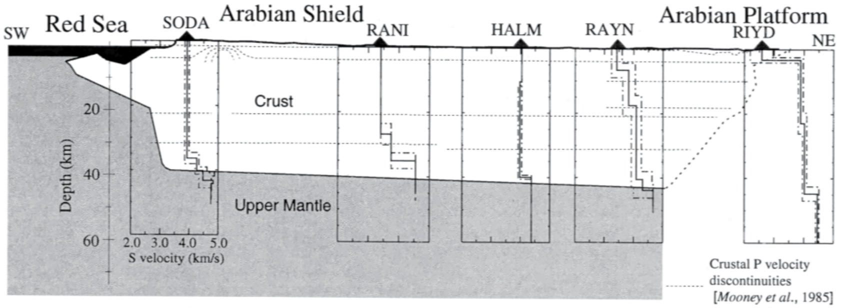

Figure 4. A comparison of our shear wave velocity models with the model of *Mooney et al.* [1985]. The shaded/white boundary marks the Moho boundary derived from the 1978 refraction experiment (Figure 1). Also shown are the major crustal P wave velocity anomalies (dashed lines). For the most part we observe no evidence of these boundaries; however, most of these are very subtle features (<0.15 km/s P wave velocity contrast). Only beneath station RAYN do we observe upper-crustal and mid-crustal velocity discontinuities. These features are also seen on the refraction model and correspond to substantial velocity contrast (~0.3 km/s).

Receiver functions for the southern Caspian

Mangino and Priestley (1998) GJI

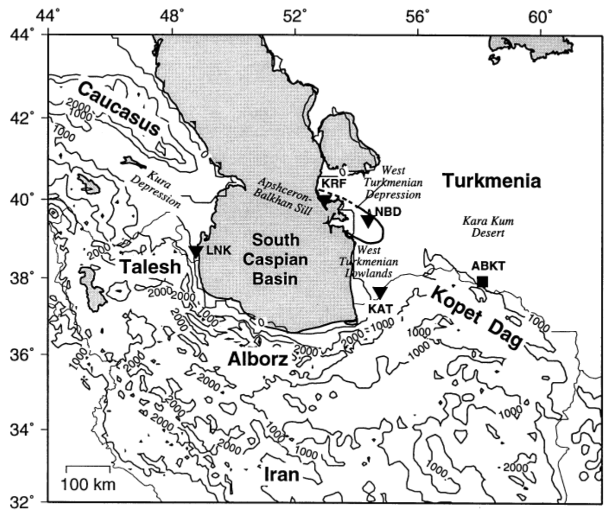

Figure 1. Topographic map of the south Caspian basin and surrounding region. Elevation varies from ~ 30 m below sea level in the Caspian to over 2 km above sea level in the adjacent mountains. The contour interval is 1000 m; solid triangles denote the Caspian Seismograph Netw stations used in this study. In Turkmenia the stations used are located at Krasnovodsk (KRF), Nebit Dag (NBD) and Kizyl Atrek (KAT). The only station in Azerbaijan used in this study is located at Lenkoran (LNK). The IRIS station Alibek (ABKT), Turkmenia, is shown as a solid square. The West Turkmenian depression is denoted by the 45 km Moho depth contour from Rezanov & Chamo (1969).

RFs integrated with DSS results

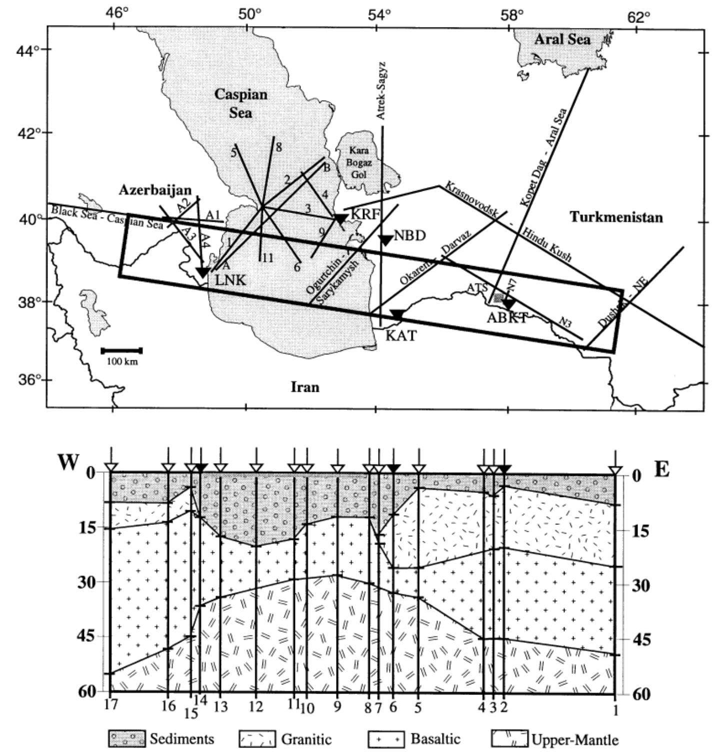

Figure 3. Cross-section of the crust and uppermost mantle (lower panel) beneath the region denoted by the box in the upper panel. Three principal crustal layers are characterized by their P-wave velocities: sediment and consolidated sediment (V_p < 4.8 km s−1), 'granitic' (V_p between 4.8 and 6.4 km s−1), 'basaltic' (V_p between 6.4 and 7.4 km s−1) and upper mantle (V_p ≥ 8.0 km s−1). Control points numbered 1–17 correspond to the following DSS (open arrows) and receiver function results (solid arrows): (1) Dushak-NE (Yegorkin & Matushkin 1970), (2) IRIS station ABKT, (3) ATS (Altyyev et al. 1988), (4) Kopet Dag–Aral Sea (Yegorkin & Matushkin 1970), (5) Okarem–Darvaz (Kurbanov & Rzhanitsyn 1982), (6) Station KAT, (7) Atrek–Sagyz (Rezanov & Chamo 1969), (8) Okarem–Darvaz (Kurbanov & Rzhanitsyn 1982), (9) Ogurtchin–Sarykamysh (Shikalibeily & Grigoriants 1980), [(10) 9, (11) 6, (12) 11, (13) 1, A–B (Aksenovich et al. 1962; Gal'perin et al., 1962)], (14) Station LNK, [(15) A4, (16) A3 (Shekinskii et al. 1967)] and (17) Black Sea–Caspian Sea (Khalilov et al. 1987).

Joint Inversion of Receiver Functions and Surface Waves

Julià et al. (2000) GJI

$$E_{y|z} = \frac{p}{N_y} \sum_{i=1}^{N_y} \left(\frac{y_i - \sum_{j=1}^{M} Y_{ij}\, x_j}{\sigma_{y_i}} \right)^2 + \frac{1-p}{N_z} \sum_{i=1}^{N_z} \left(\frac{z_i - \sum_{j=1}^{M} Z_{ij}\, x_j}{\sigma_{z_i}} \right)^2 . \qquad (8)$$

Receiver Functions — **Surface Waves**

Another “classic”

Seeks to deal with the non-uniqueness of RFs with the inclusion of surface wave dispersion

Comparison to refraction results

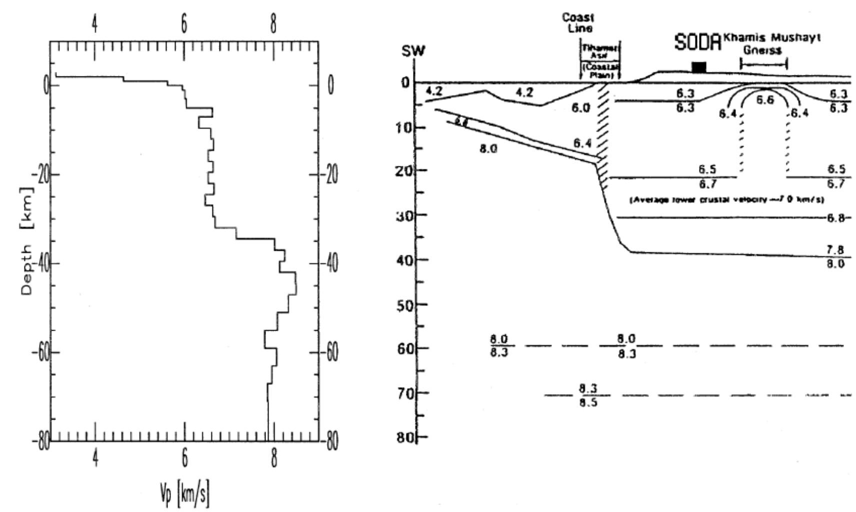

Figure 13. Comparison between the preferred model (left) inferred from the joint inversion expressed in terms of *P*-wave velocities, and the cross-section (right) interpreted from the refraction profile of Mooney *et al.* (1985). Note that the vertical scale in the resulting model has been shifted to match that in the cross-section.

Western Arabia

Julià et al. (2003) Tectonophysics

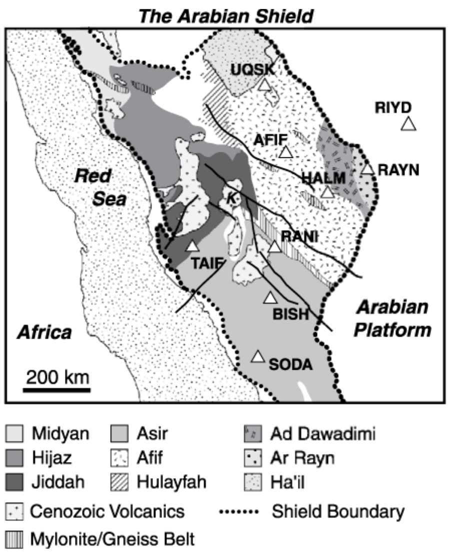

Fig. 1. Terrane map of the Arabian Peninsula showing the location of nine temporary stations in the Saudi Arabian Portable Broadband Deployment (triangles) superimposed on regional geologic terranes and suture zones defined in Johnson (2000) Also shown are the locations of Cenozoic surface volcanics. Harrat al Kishb, the site of thermobarometry information is labeled with a "K".

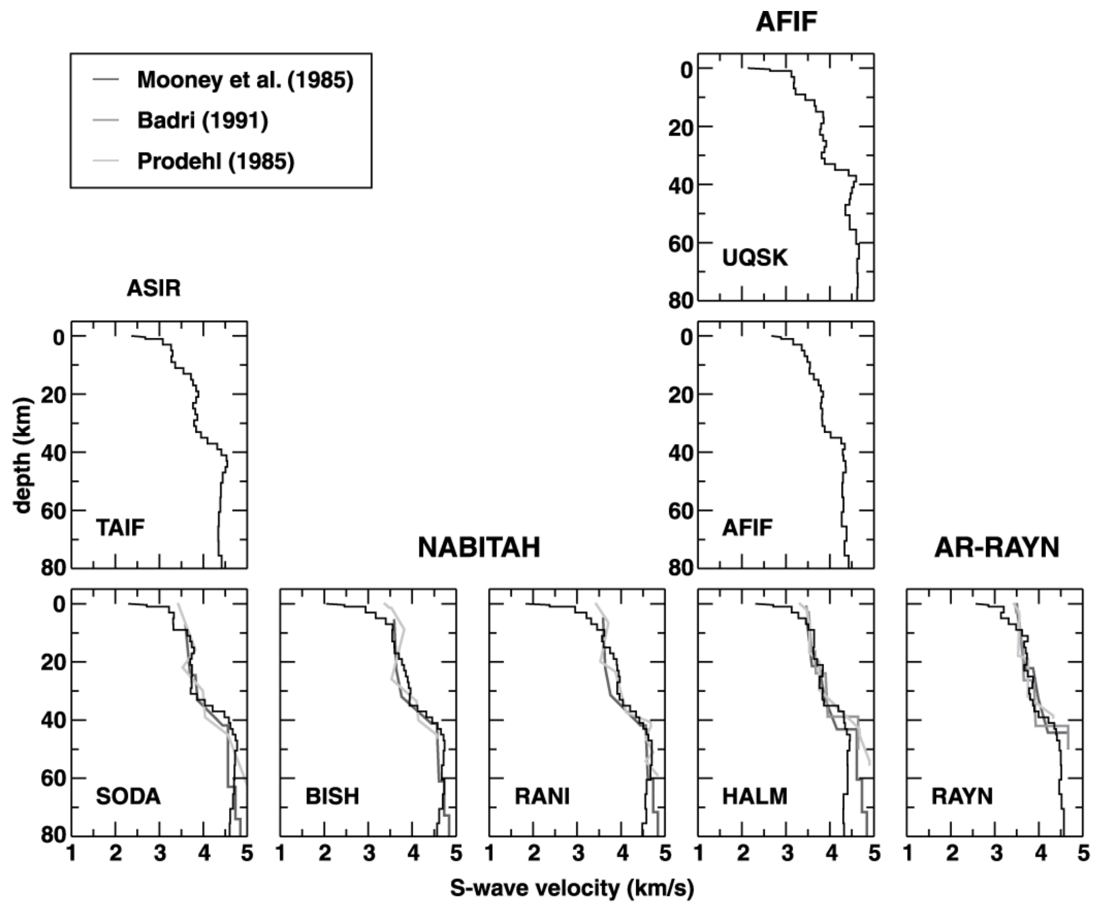

Fig. 7. Summary plot of S wave velocity models in the Arabian Shield, and comparison to refraction profiling results (bottom). Note that the distribution of the models resembles that of the stations in Fig. 1.

Back to Saudi PASSCAL

Eastern Turkey

Zor et al. (2003) GRL

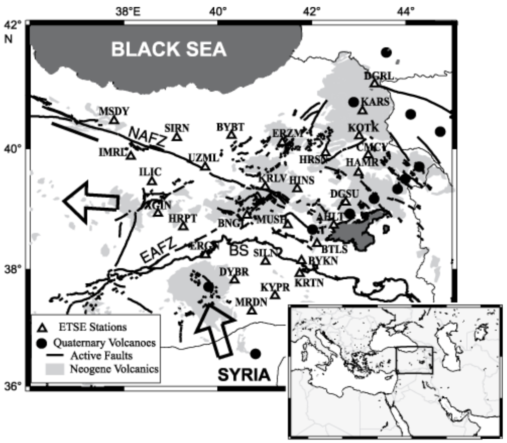

Figure 1. Map showing the 29 three-component PASS broadband stations (triangles) used in the Eastern T Seismic Experiment (ETSE). Filled circles indicate Quat nary volcanoes and the gray shaded area shows Ne volcanics. Arrows indicate the direction of the plate anc motions. BS, NAFZ, and EAFZ are the Bitlis-Zagros sutu zone, North Anatolian fault zone, and East Anatolian zone, respectively.

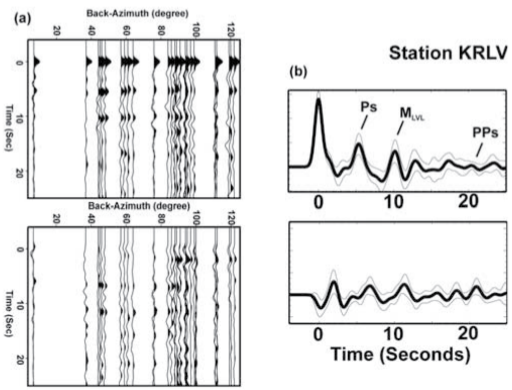

Figure 2. (a) Section of 27 single-event radial (top) and
or KRLV station,
(b) Stacked radial
unctions and thei
represent the
nultiple, and the
e, respectively.

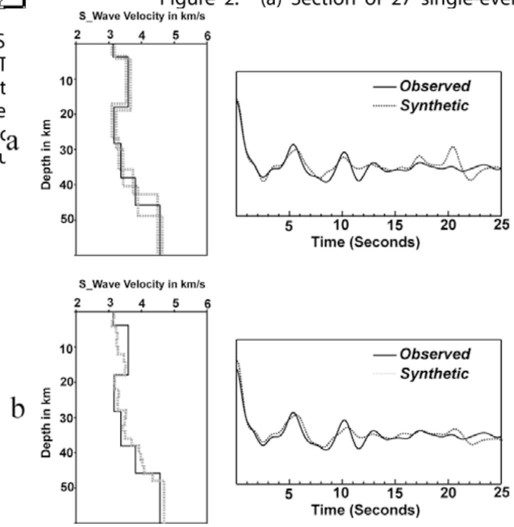

Figure 3. (a) On the left is the estimated velocity model (solid line) and its sensitivity limits (dashed lines) for KRLV station. The right panel is the waveform match between synthetic (dashed) and the observed (solid) receiver functions. (b) Many layered linearized inversion results (dashed line) on the left. The grid search results (solid line) were used as an initial model. The improvement of the waveform match is shown on the right.

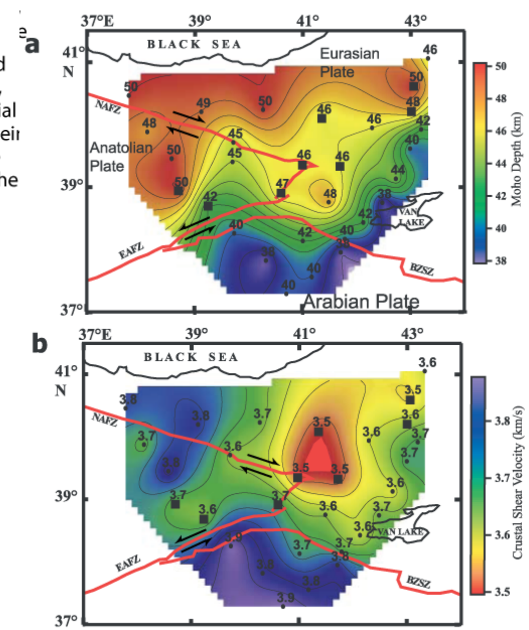

Figure 4. Maps showing (a) the Moho depth variation in km (contour interval is 1 km) and (b) the average crustal shear velocity in km/s (contour interval is 0.04 km/s) for each station. Black squares indicate stations which may have a low velocity layer. Red lines indicate the three plate boundaries.

Eastern Turkey Seismic Experiment (ETSE) PASSCAL deployment

Jordan

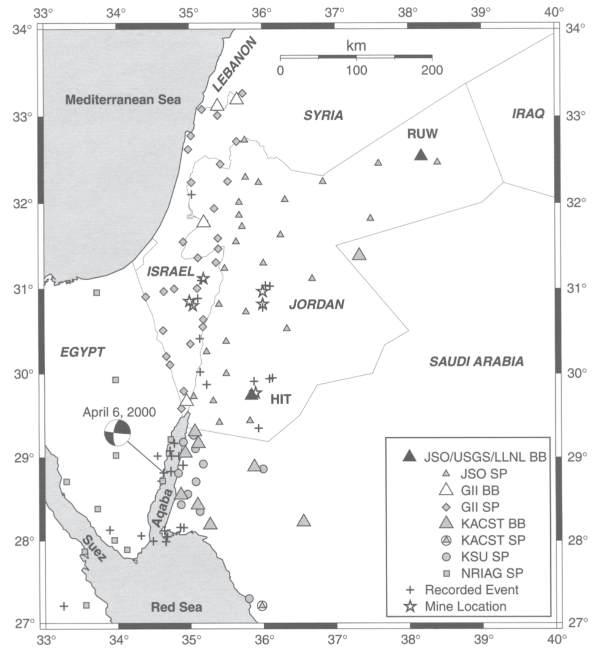

Rodgers et al. (2003) SRL

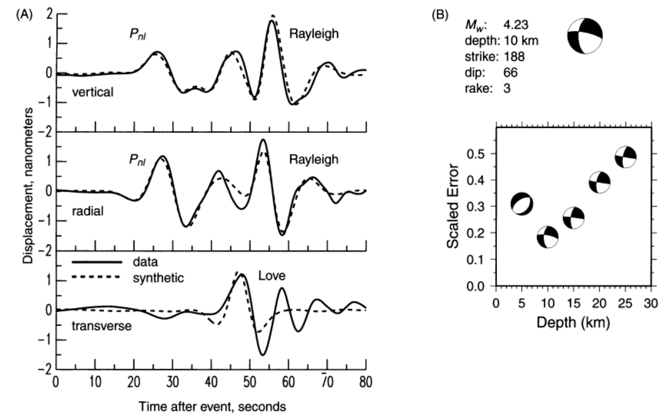

▲ **Figure 2.** Source parameter estimation of the 6 April 2000 Gulf of Aqaba earthquake from long-period waveforms recorded at HIT. The event location is shown in the map in Figure 1. (A) Waveform fits between data (solid) and synthetic (dashed) for the period band 10–50 seconds. (B) Mechanism and misfit as a function of event depth. The best fit is a left-lateral strike-slip mechanism at 10 km depth.

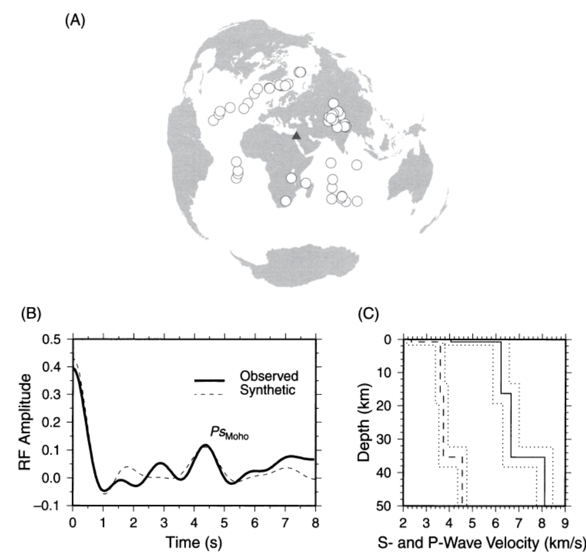

▲ **Figure 3.** Teleseismic receiver function (RF) analysis at HIT. (A) Events used in RF stack. (B) Observed (solid) and synthetic (dashed) RF stack (maximum frequency 1.0 Hz). Note the prominent *P*-to-*S* converted phase at about 4.2 s (*Ps*-Moho). (C) The estimated velocity structure and uncertainty.

Model also used in waveform inversion

Dead Sea Fault

Moshen et al. (2005) GJI

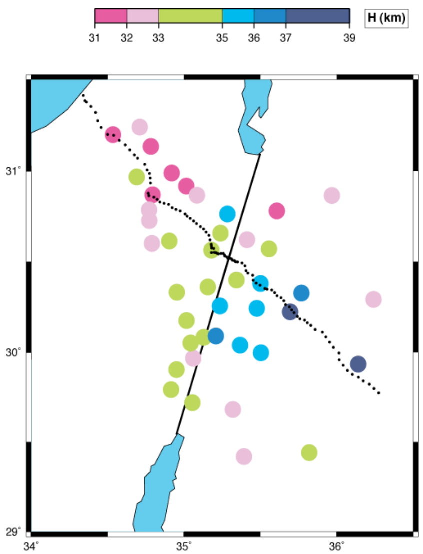

Figure 6. Map of Moho depth values from Fig. 5 and Table 1.

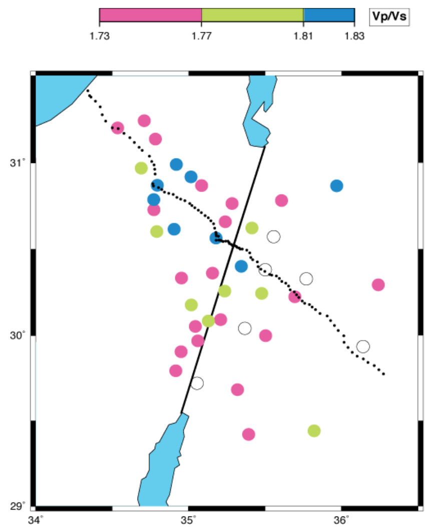

Figure 7. Map of V_p/V_s ratios from Fig. 5 and Table 1. Open circles represent stations for which the V_p/V_s ratio has not been determined.

Comparison with results from reflection/refraction

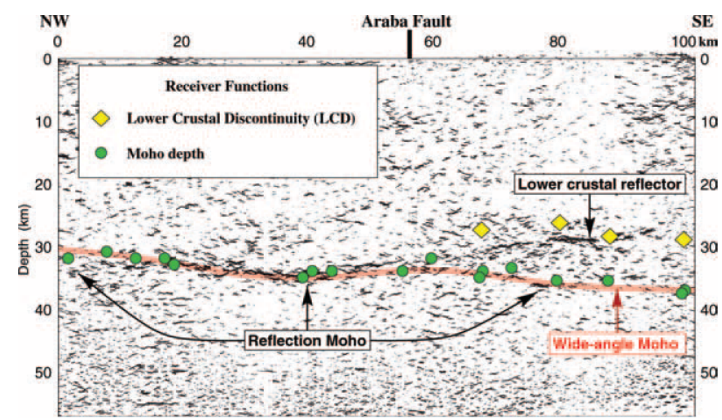

Figure 10. Comparison of depth determinations of the Moho and Lower Crustal Discontinuity by steep- and wide-angle controlled-source techniques and receiver functions. The error in the Moho depth determined with receiver functions is estimated at less than 1 km at most stations (see Table 2).

Arabian Peninsula

Al-Damegh et al. (2005) EPSL

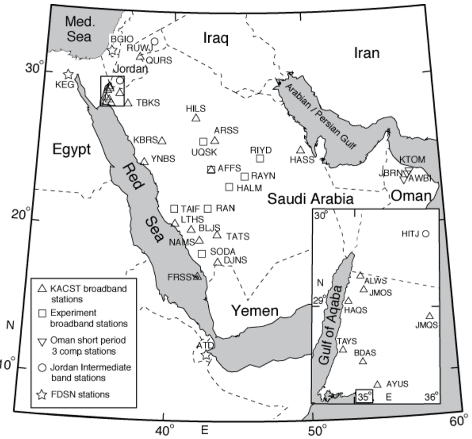

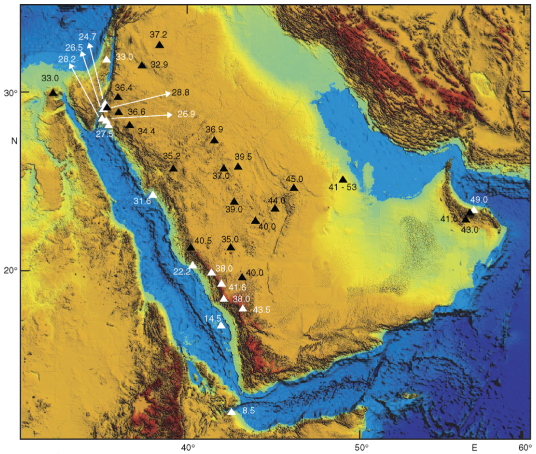

Fig. 2. Map showing the seismic stations used in this study. In addition, the map shows stations in the region for which receiver function results were discussed in the text (squares, stars, and downward triangles). The inset shows stations along or close to the Gulf of Aqaba.

More of the Arabian Peninsula

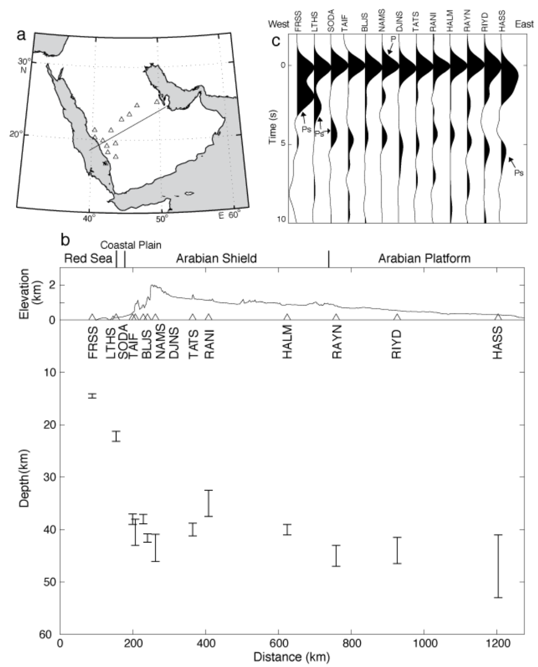

Fig. 11. Map and cross-sections showing Moho depth at stations along a profile from the Red Sea to the east coast of Arabia. (a) Map showing the location of the profile. (b) The cross-section with vertical exaggeration. (c) Stacked radial receiver functions for distances 30–85° for the same stations shown in the cross-section (b).

Arabia

Tkalčić et al. (2006) JGR

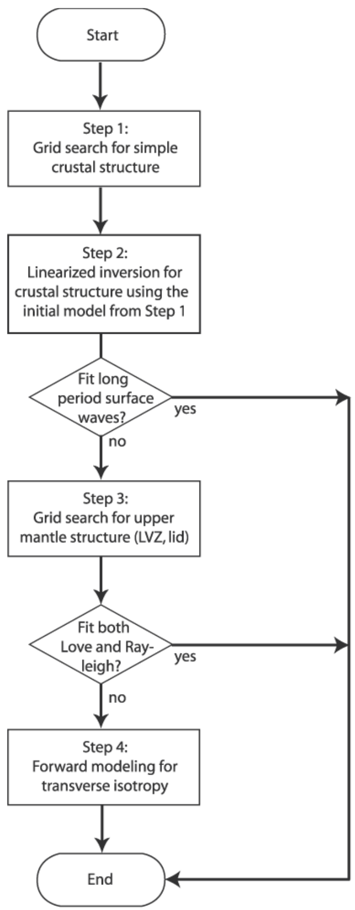

Figure 5. A flowchart demonstrating the four steps of the MSA4 method.

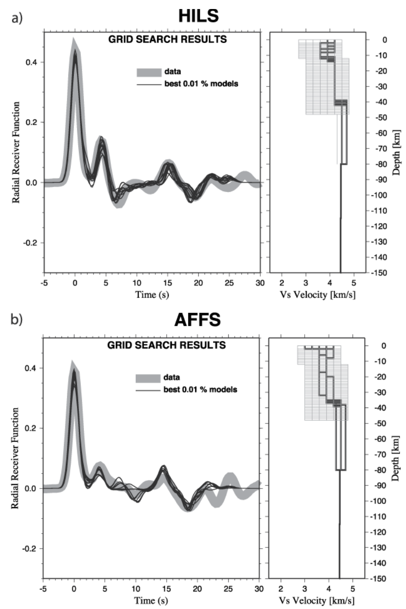

ure 6. Grid search results for lithospheric structure after modeling the observed receiver functions for ow-pass Gaussian filter width parameter a = 1.0 for (a) HILS and (b) AFFS, two stations located in the ıbian Shield. Thick gray line is a stacked and averaged observed receiver function and thin black lines : (left) modeled receiver functions and (right) corresponding shear wave velocity profiles for the best 1% models obtained in the grid search. The range of grid search is shown on the right by thin gray lines.

RFs only

Do they fit SWs?

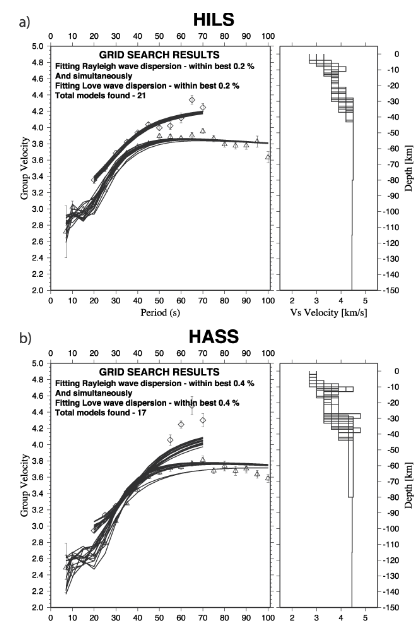

Figure 7. Grid search inversion results for lithospheric structure after modeling the observed Rayleigh wave (triangles) and Love wave (diamonds) group velocity dispersion at HILS and AFFS, the two stations also shown in Figure 6. Black lines are (left) modeled dispersion curves and (right) corresponding shear wave velocity profiles for the best 0.2% (for HILS) and 0.4% (for AFFS) models obtained in the inversion. The ±1 standard deviation bars are shown on SWGV data.

Arabia - continued

Tkalčić et al. (2006) JGR

Which models fit the surface waves?

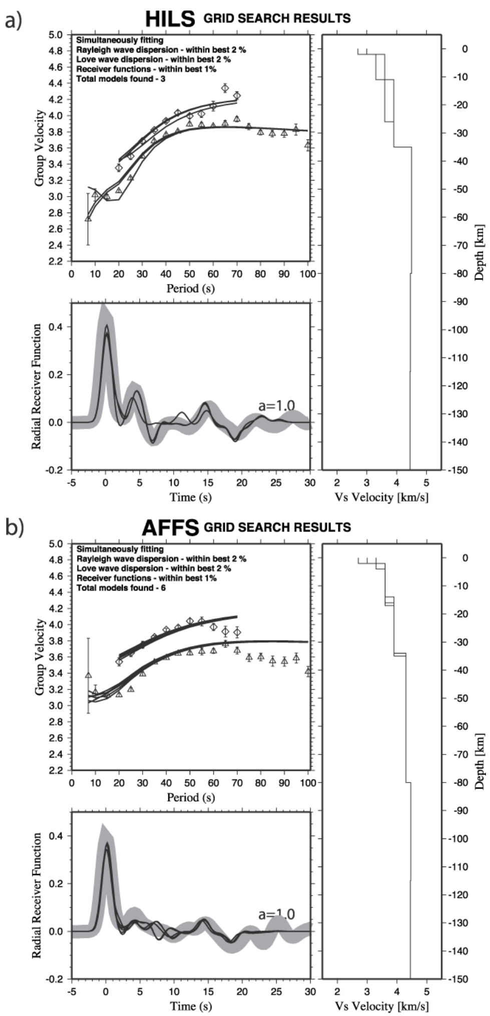

Figure 8

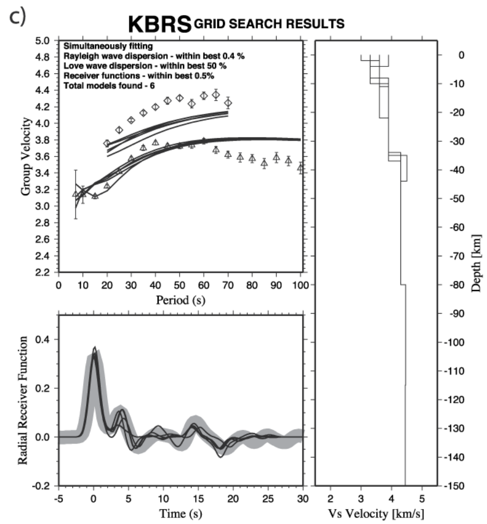

Figure 8. (continued)

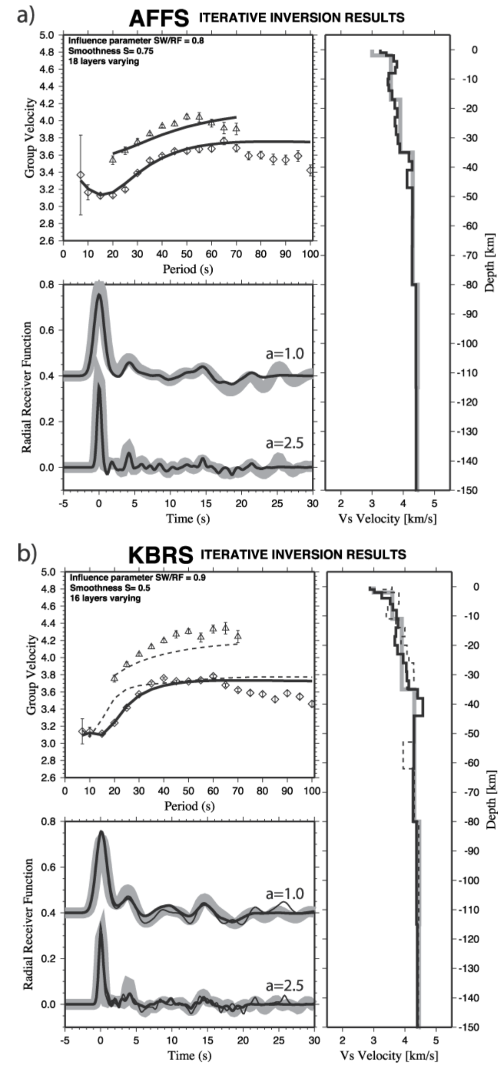

Figure 9

Are SWs fit with mantle half-space?

Arabia - continued

Tkalčić et al. (2006) JGR

Mantle Low Velocity Zone (LVZ)

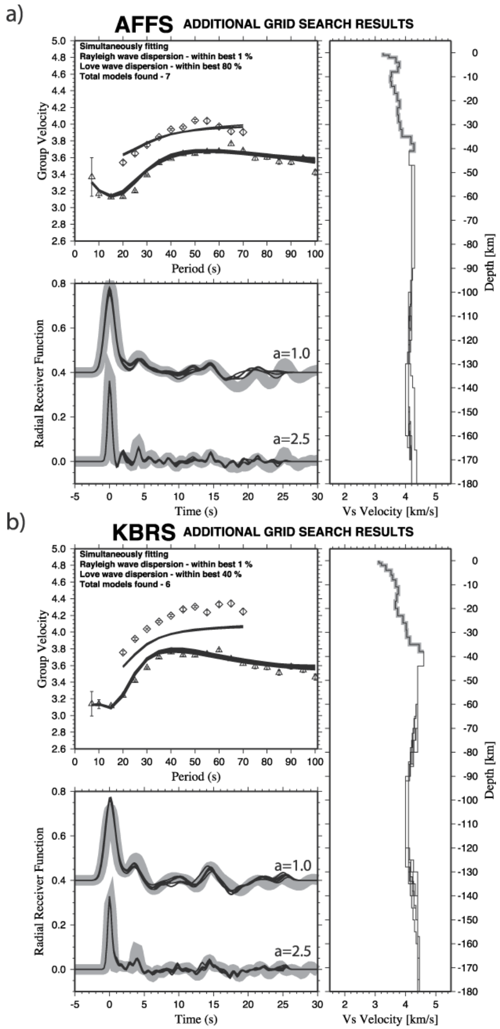

Figure 10

Transverse Isotropy in Mantle

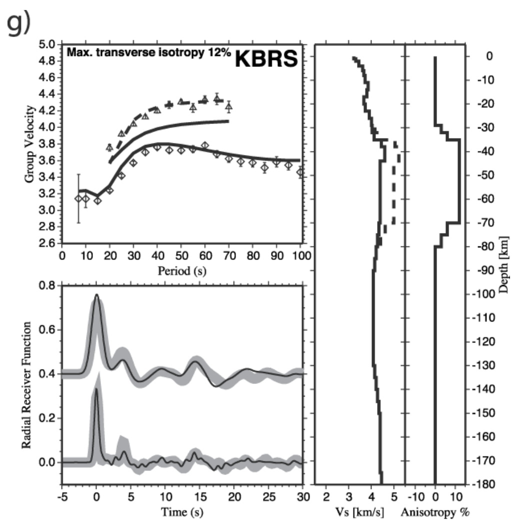

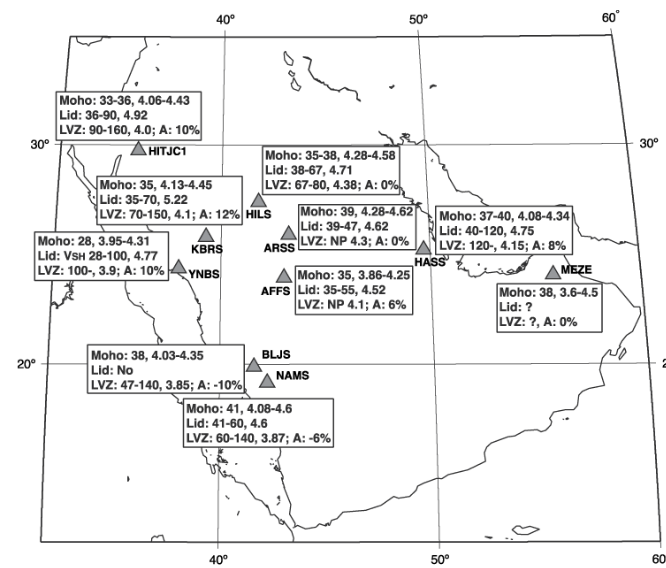

Figure 12. Map of station locations (triangles) and the values estimated in the modeling presented in Figures 11a–11e. Line 1 is Moho depth, shear wave velocity values in the layer above and the layer below Moho; line 2 is lithospheric lid thickness, maximum shear wave velocity in the lid (v_{SV} or v_{SH}); line 3 is thickness of the low-velocity zone (NP, not pronounced), minimum shear wave velocity in the LVZ (v_{SV} or v_{SH}); maximum percentage of $v_{SH} > v_{SV}$ transverse isotropy.

Zagros Mts.

Paul et al. (2006) GJI

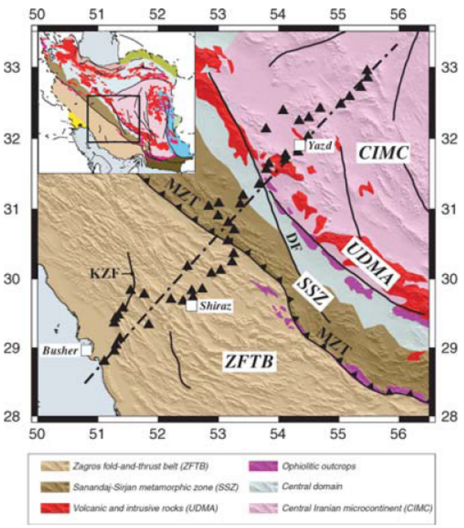

Figure 1. Location map of the seismological network. The black box on the geological map of Iran in inset shows the location of the regional map. Stations used in this study are plotted as black triangles. The dash-and-dot line is the N42 profile used in cross sections of Figs 2 and 4. The main faults are shown as thick black lines. Geological map modified from the structural map of NGDIR (National Geoscience Database of Iran, http://www.ngdir.ir). MZT: Main Zagros thrust; KZF: Kazerun fault; MZT: Main Zagros thrust and DF: Deshir fault.

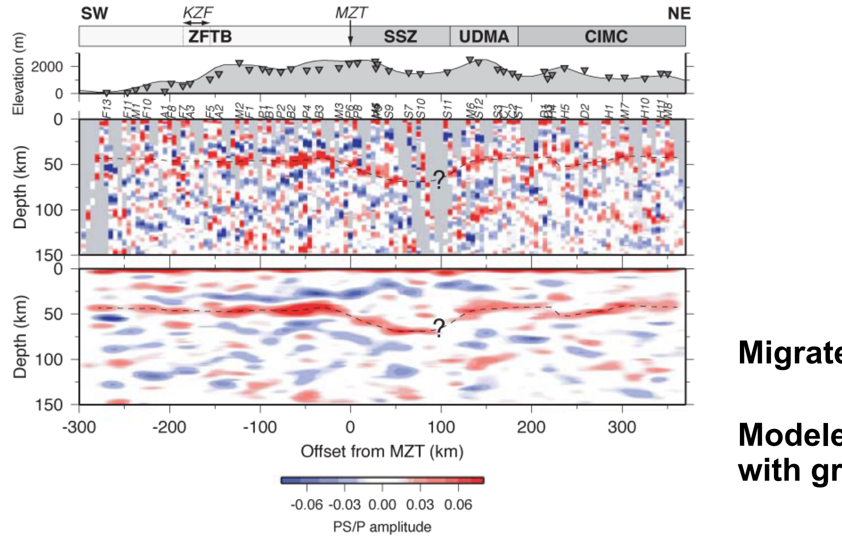

Figure 4. Migrated depth section computed from radial RFs along the N42 profile. The blue-to-red colour map displays the average amplitude ratio of the Ps converted phase to the primary P for all rays crossing the bin. Top: average elevations along the N42 profile; inverted triangles show heights of seismological stations. Middle: raw migrated depth section. Empty bins (without a single ray) are plotted in light grey. The dotted line is the Moho depth profile picked from the smoothed depth section. Bottom: migrated depth section after filtering and smoothing.

Migrated RFs

Modeled in conjunction with gravity

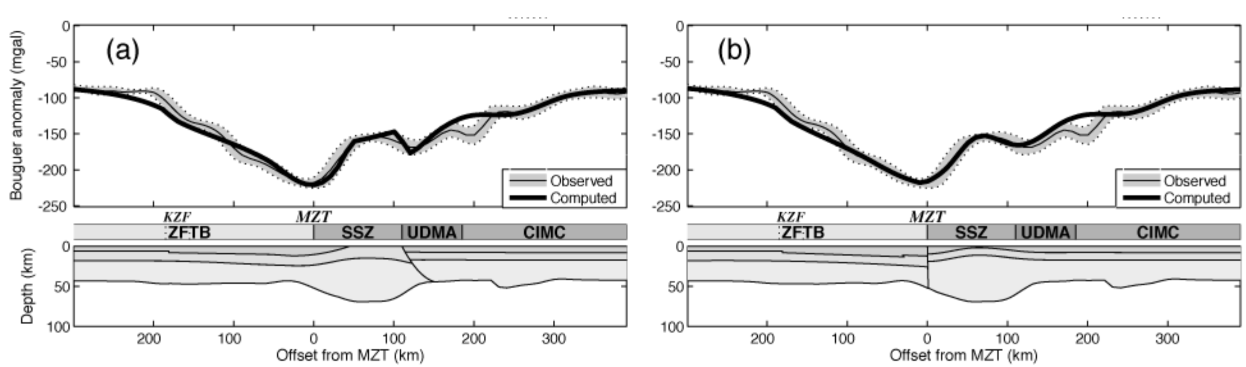

Figure 7. Results of 2-D gravity modelling for: (a) a crustal model with the suture located at the boundary between the SSZ and the UDMA (Alavi, 1994), (b) a crustal model with an Andean-type thickened margin beneath the SSZ. Same legend as Fig. 6.

Eastern Turkey – S-wave receiver functions

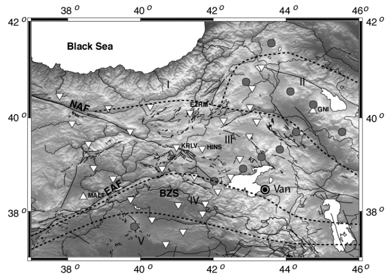

Figure 2. Map showing the location of the 29 three-component PASSCAL broadband stations in the ETSE array (inverted triangles), the two permanent stations GNI (GSN-IRIS/USGS network) and MALT (GEOFON network) (triangles) and Holocene volcanoes (circles). Abbreviations: NAF, North Anatolian Fault; EAF, East Anatolian Fault; BZS, Bitlis–Zagros Suture Zone. Approximate location of the major tectonic units of eastern Turkey are shown (modified fro Keskin 2005): (I) Rhodope-Pontide fragment, (II) Northwest Iranian fragment, (III) Eastern Anatolian Accretionary complex (EAAC), (IV) Bitlis–P oturge Massif and (V) Arabian foreland.

Angus et al. (2006) GJI

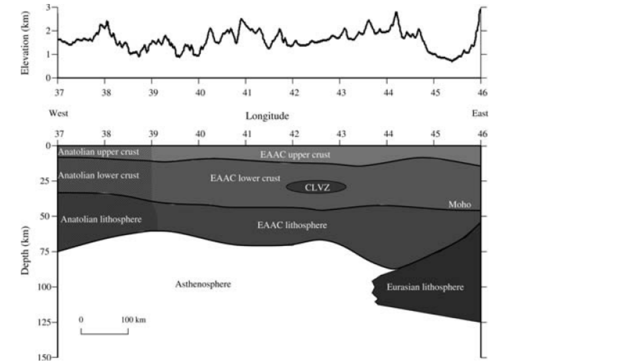

Figure 9. Top: Topographic relief of eastern Turkey at 39N. Bottom: sketch illustrating the collision of the Arabian and Eurasian plates summarizing the results of S-receiver function analysis for an east–west cross section at 39N.

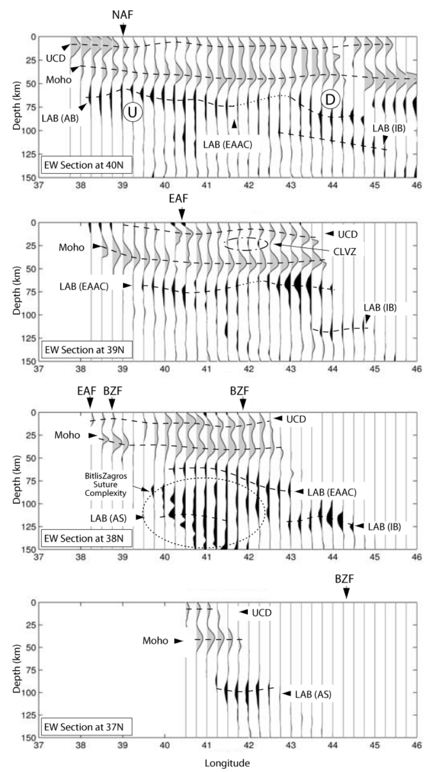

Look at deeper lithospheric structure with SRFs

Figure 4. East–west profiles at 37, 38, 39 and 40N. In this and the remaining figures, the dashed lines are the inferred seismic discontinuities for the crust and upper mantle. The dotted lines indicate regions where the LAB is very weak. The dotted ellipse, in this and the remaining figures, highlights the reg where the Bitlis–Zagros suture zone (BZSZ) is believed to introduce complexity in the receiver function images. A dashed-dotted ellipse indicates crustal low velocity zone (CLVZ). The letter U highlights a region of thin lithosphere (also seen in Fig. 5) and the letter D a region of thick lithosphere. Abbreviations: UCD, upper-crust discontinuity; LAB, lithosphere–asthenosphere boundary; EAAC, East Anatolian accretionary complex; AS, Arabian Shield; IB, Iranian Block. The location where the vertical profile crosses a major fault zone is indicated along the top. Note: straight lines in Figs 4–7 do not indicate seismic signal, but rather lack of data.

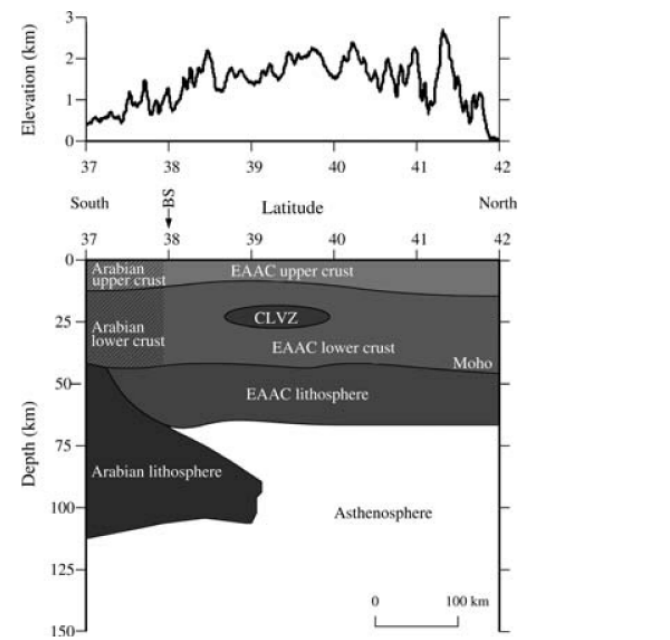

Figure 10. Top: Topographic relief of eastern Turkey at 42E. Bottom: sketch illustrating the collision of the Arabian and Eurasian plates summarizing the results of S-receiver function analysis for a north–south cross section at 42E.

Kuwait

Pasyanos et al. (2007) JGR

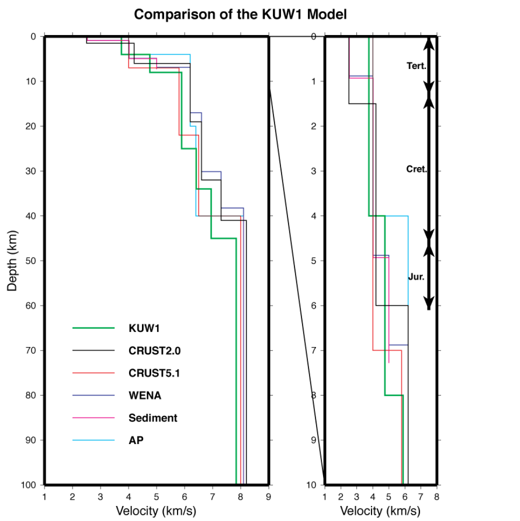

Figure 9. The KUW1 velocity model and other nearby velocity models. The KUW1 model is shown in green. Other models are as follows: CRUST2.0 in black, AP model in cyan, WENA model in blue, sediment model in magenta, and the Kuwait model (from CRUST5.1) in red. Arrows to the right show the sedimentary column from Bou-Rabee (2000).

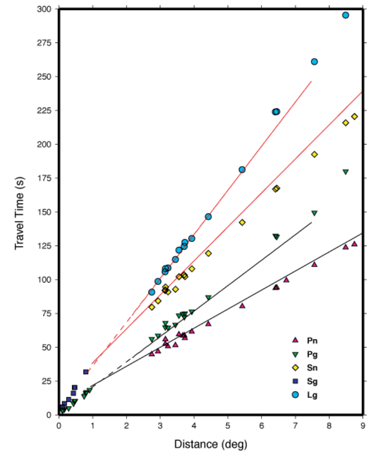

Figure 10. Traveltimes of Pn (triangles), Pg (inverted triangles), Sn (diamonds), Sg (squares) and Lg (circles) phases for local events and regional events from the Zagros Mts recorded at station KBD. Traveltime fits to the data from model KUW1 are shown in solid and dashed lines.

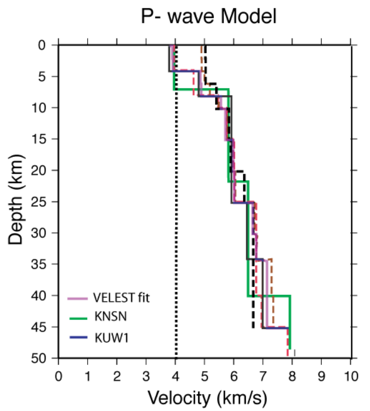

Figure 11. P-wave velocity results for Kuwait from local seismicity. The blue line is the KUW1 model and the green line is the model originally used to locate events in the region. Dashed lines are outputs of VELEST program using various input models. Based on the range of output model, the velocities between 8 and 20 km are resolvable. The purple line is the final model from the VELEST inversion, which compares favourably to the KUW1 model.

RFs with local and teleseismic travel times

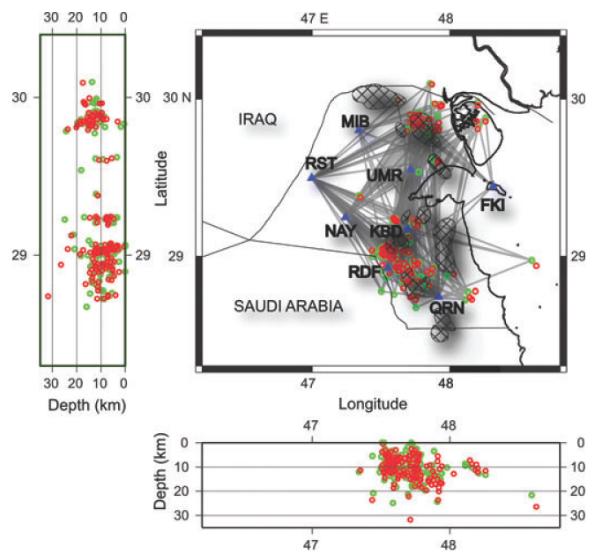

Figure 12. Original (green circles) and relocated (red circles) epicentres. Ray paths between stations (blue triangles) and earthquakes are shown as grey lines. Events are concentrated in the northern and southern oilfields (shown as hatched areas).

Eastern Turkey – Joint Inversion

Gök et al. (2007) JGR

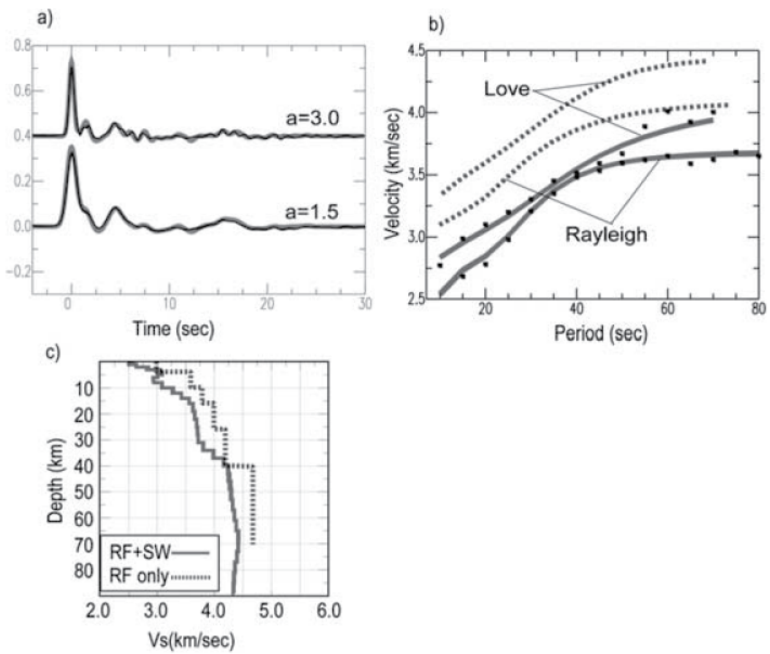

Figure 4. A comparison between the RF-only inversion and the joint RF-SW inversion. (a) receiver functions (a is Gaussian filter), (b) dispersion curves and (c) velocity models. The RF-only model (dotted lines) was unable to fit the SWs, but the joint technique was able to fit them without any degradation to the RF fit.

Same RFs as Zor et al. (2003)

Illustrates the large non-uniquenesses in RF only inversions

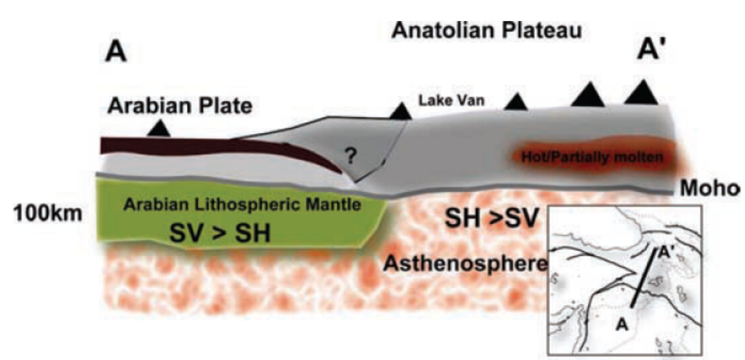

Figure 10. The schematic diagram of N-S trending profile showing the proposed lithospheric structure in eastern Turkey. As indicated by the velocity and anisotropy in our study, there is no indication of lithospheric mantle in the plateau.

Iraq – Joint Inversion

Gök et al. (2007) GJI

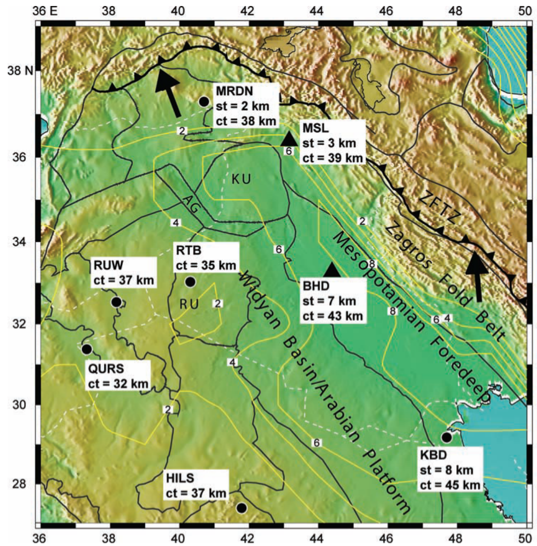

Figure 1. Base map of the study region including the locations of seismic stations BHD and MSL (triangles). Adjacent stations (RTB, MRDN, KBD, RUW, QURS and HILS, circles) have reported crustal structures. Tectonic provinces are indicated (black lines). Major features in Iraq are identified and also include the Khleisha Uplift (KU), Anah Graben (AG), Rutbah Uplift (RU) and Main Zagros Thrust (MZT), taken from Pollastro et al. (1997a,b). Sedimentary thickness across the region is plotted as yellow contours (Bassin et al. 2000). Summary of crustal and sedimentary thickness (ct and st, respectively) at stations BHD and MSL. Note that the crystalline crustal thickness (ct-st) for stations along the northeastern Arabian Platform (KBD, BHD, MSL and MRDN) is very consistent at about 36 km. Also shown are results for nearby stations referred to in the text.

Thicker crust in areas with thicker sediments – same thickness of crystalline crust

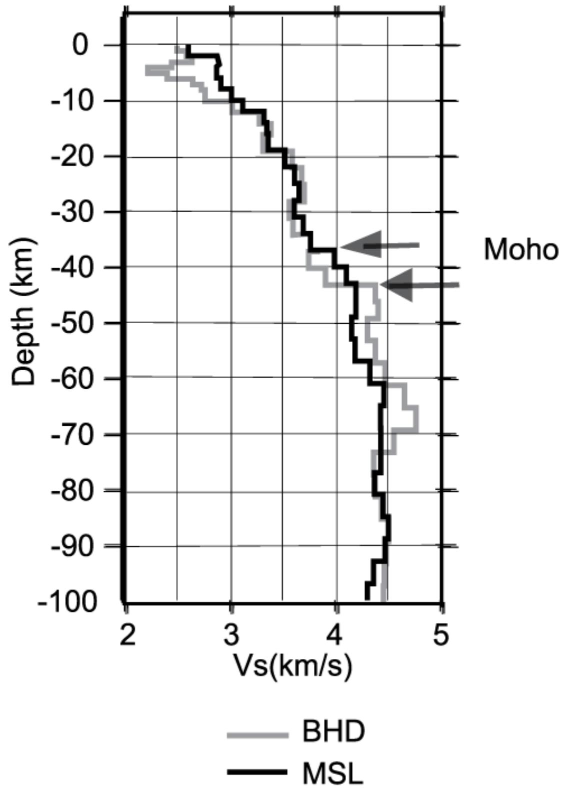

Figure 6. Comparison of the shear velocity profiles at station BHD (grey) and MSL (black). Arrows indicate the estimated Moho depths for each profile.

Arabia – S-wave receiver functions

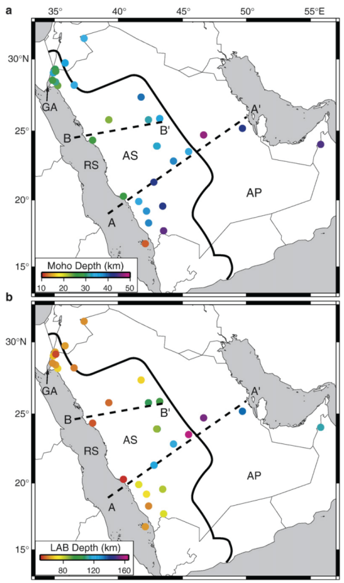

Fig. 4. Maps showing the boundary depths beneath Arabia. The colored circles show a Moho and b LAB depths beneath individual stations where warmer colors indicate shallower depths than cooler colors. The solid line marks the boundary between the Arabian Shield (AS) and the Arabian Platform (AP) while the two dashed lines mark the locations of cross-sectional profiles AA′ and BB′ in Figs. 5 and 6. RS: Red Sea, GA: Gulf of Aqaba.

Hansen et al. (2007) EPSL

S-wave receiver functions useful for estimating lithospheric thickness

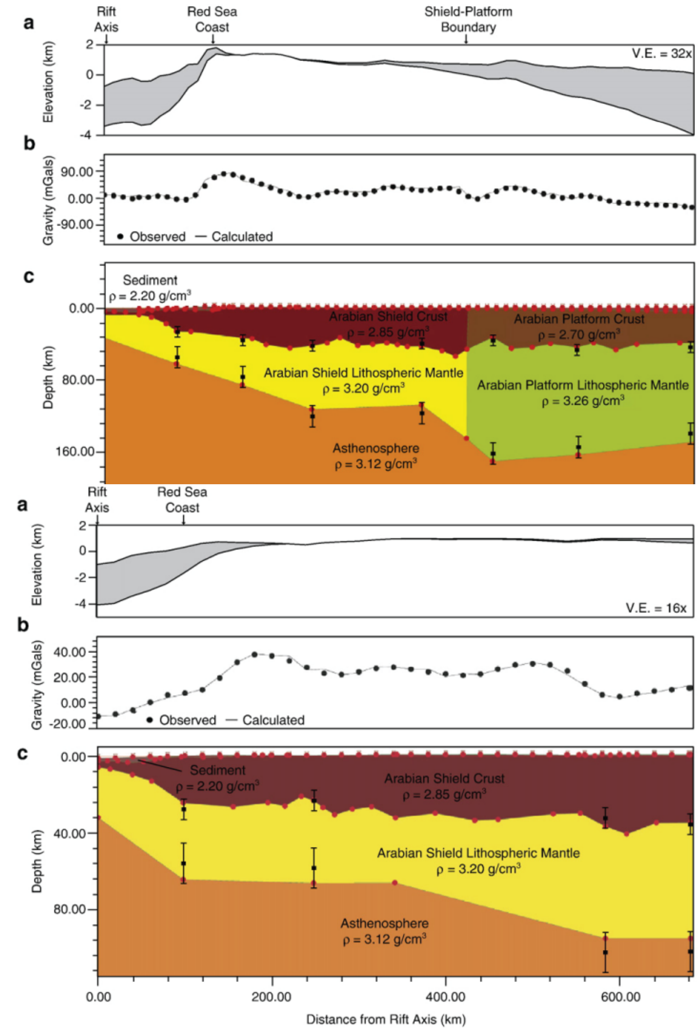

Fig. 6. Topography, gravity signature, and lithospheric structure along cross-sectional profile BB′ from Fig. 4. a Topography along the profile plotted with a 16× vertical exaggeration (V.E.). The sediment thickness is shown by the grey shaded area. b Comparison of the observed gravity data from the GRACE satellites (black dots) and the calculated gravity (grey line) resulting from the structural model shown in c. Red dots in c mark nodes that were used in the gravity modeling to constrain the boundary depths, and the densities (ρ) of each layer are listed. For stations along the profile, the Moho and LAB depths from the SRF analysis are shown by black squares with error bars. The depth errors on the Moho and LAB were 5 and 10 km, respectively, and the boundary depths in the gravity model are well within the error estimates.

Oman – Joint Inversion

Al-Hashmi et al. (2011) GJI

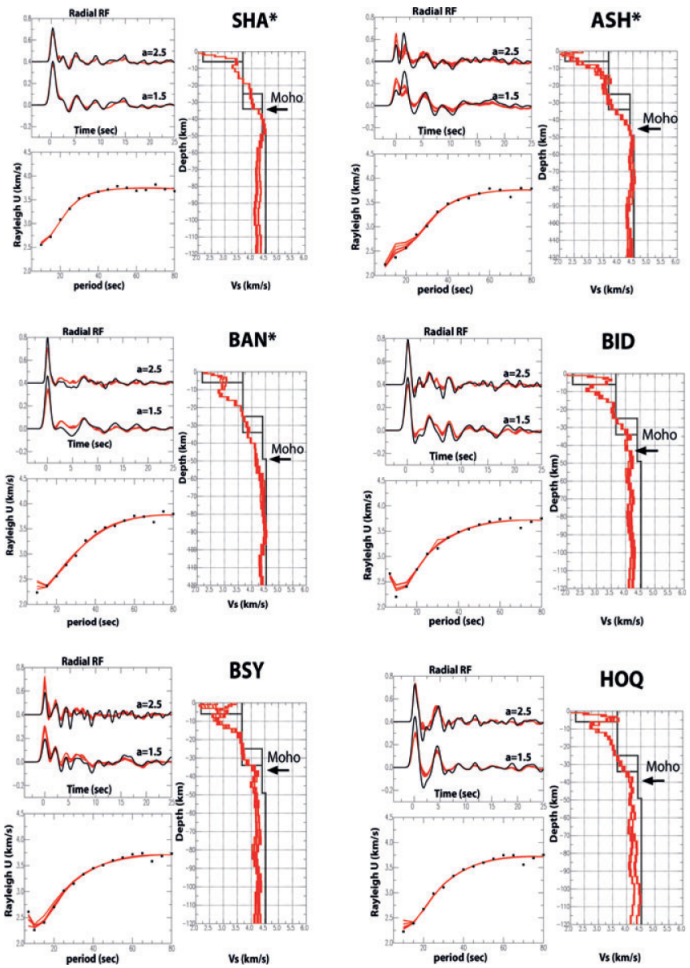

Figure 4. (a) The inversion results for six stations. The black line is the data and reds are synthetic. Two starting models along with various influence parameters (p = 0.3, 0.5 and 0.7) and smoothness (0.6 and 0.7) used to obtain the final output. The sensitivity of the inversion is mostly observed at noisier stations e.g. BSY and HOQ. (*) indicates broad-band stations. (b) The inversion results for seven stations. The black line is the data and reds are synthetic. Two starting models along with various influence parameters (p = 0.3, 0.5 and 0.7) and smoothness (0.6 and 0.7) used to obtain the final output.

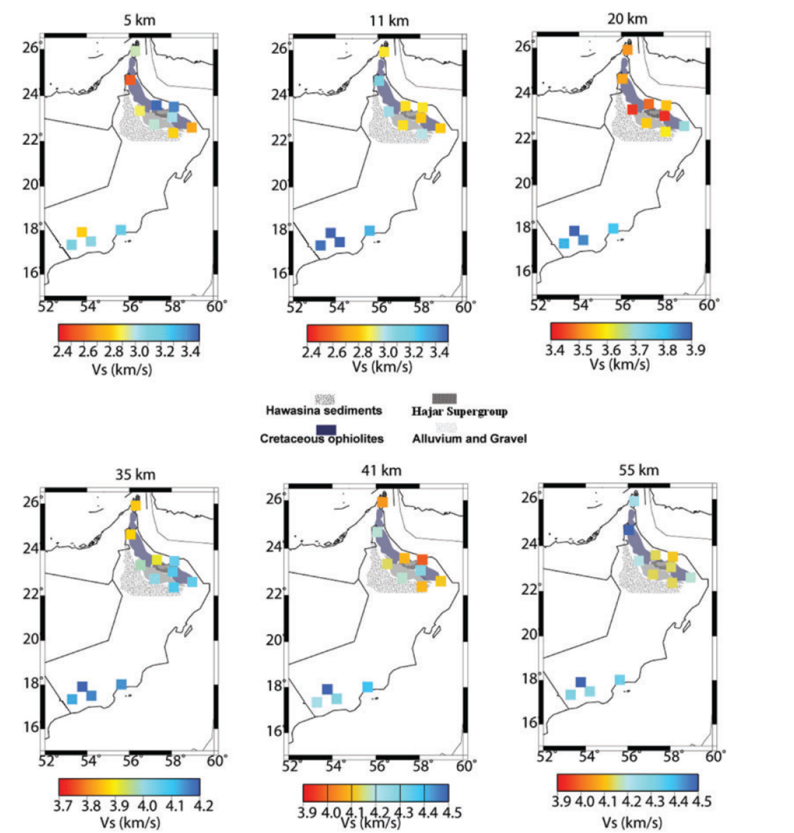

Figure 6. The shear wave velocities at various depths to present upper, lower crust and upper mantle velocities. The geologic units are shown with various patterns on each map.

Example of using different filters (a=1.5, a=2.5) to achieve better depth sensitivity

Eastern Turkey and Caucasus – Joint Inversion

Gök et al. (2011) JGR

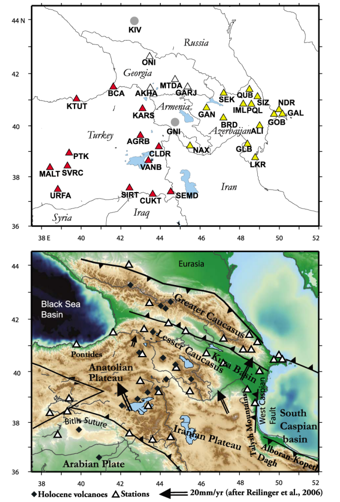

Figure 1. (top) Stations that contributed data to this study. Stations are colored by country (Turkey, red; Georgia, white; Azerbaijan, yellow; Global Seismographic Network stations, gray circles). (bottom) Tectonic features of stations in Figure 1 (top).

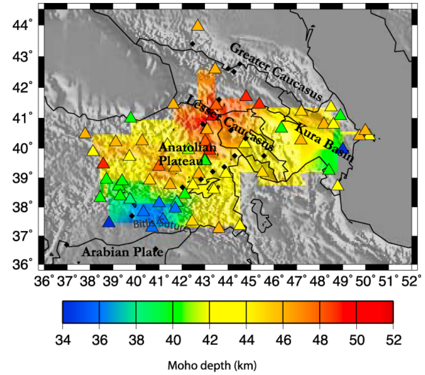

Figure 5. Interpolated Moho depths of this study including Moho depth results from the Eastern Turkey Seismic Experiment (ETSE) network [Gök et al., 2003]. The deepest Moho is observed in the Lesser Caucasus region, and the shallowest is in the Arabian plate.

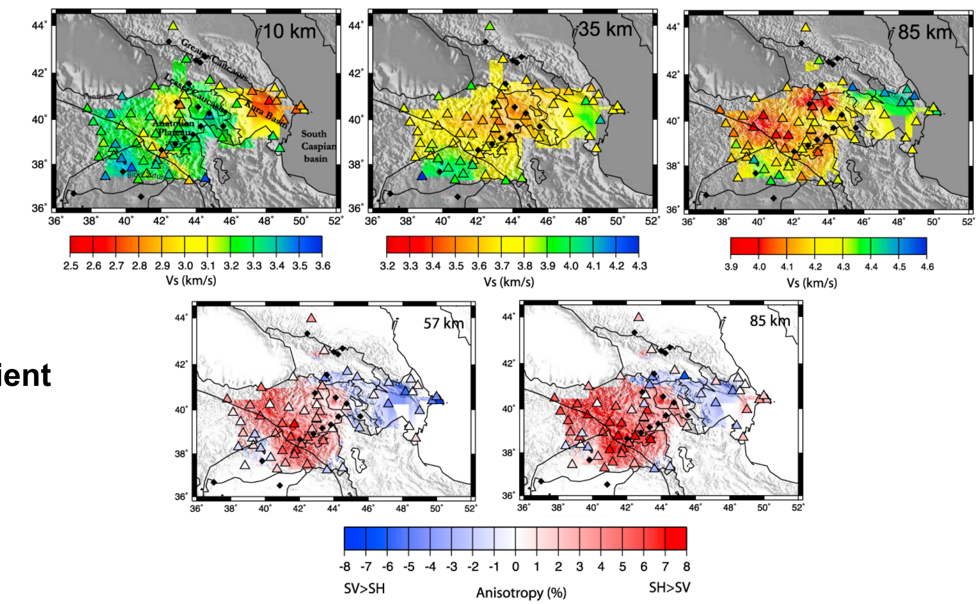

Figure 6. (top) Horizontal slices of velocities at upper crust (10 km), lower crust (35 km), and upper mantle (85 km). Small black diamonds show locations of Holocene volcanics. Thick sediments of Kura basin are still prominent at 10 km depth. Slowest velocities within the lower crust and upper mantle are observed in northeast Anatolian plateau and Lesser Caucasus. The lower crust in the Kura basin is relatively fast. (bottom) Maps showing anisotropies at 57 and 85 km depth.

Uses surface wave dispersion from both event-based and ambient noise methods

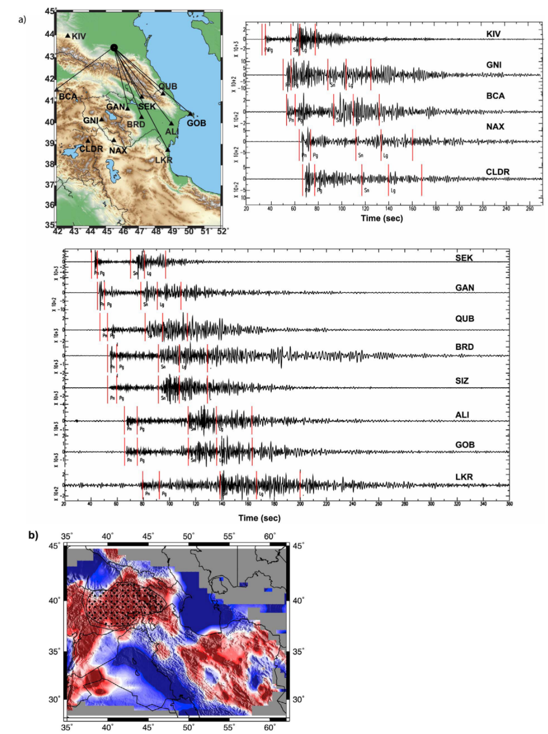

Figure 7. (a) An example event showing the propagation efficiencies of Sn and Lg. (b) Sn propagation efficiency tomography. Red is blocked Sn, and blue is efficiently propagating Sn. The shaded area is the low-velocity anomaly at 85 km (Figure 6).

Mesopotamian Foredeep – Joint Inversion

Figure courtesy of
Rengin Gök

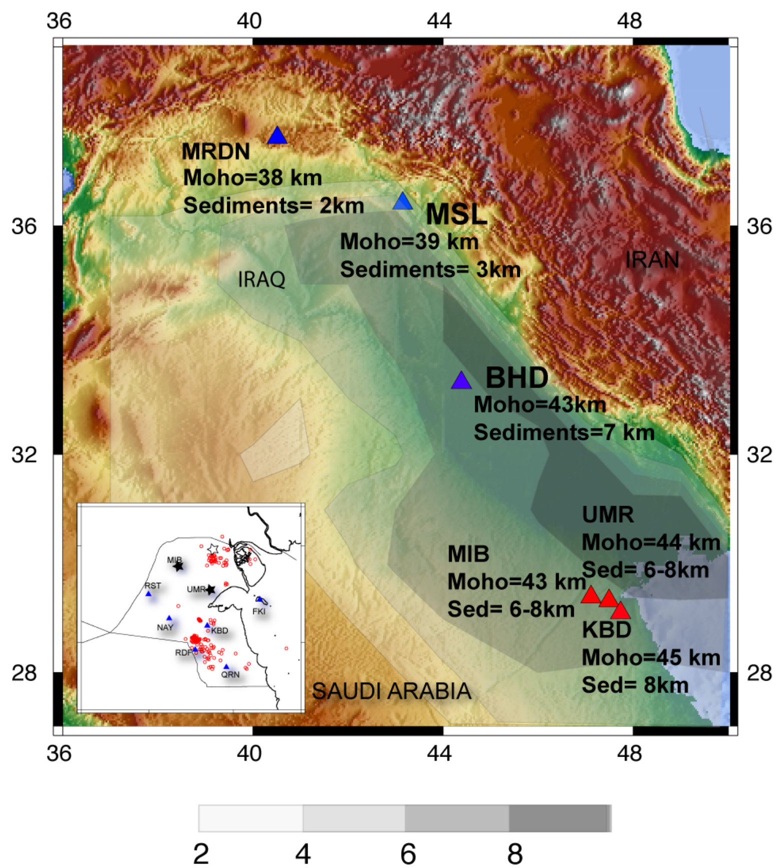

Sediment thickness (Laske and Masters, 1997)

Revisiting Mesopotamian Foredeep with stations in Kuwait –

Thicker sediment + Same crystalline crust = Thicker overall crustal thickness

Conclusions

Teleseismic receiver functions are a well-established method for recovering earth structure.

Receiver function methods are becoming more sophisticated with time.

Much improvement is a result of access to more datasets.

Analysis is becoming more “broadband”.

Methods are able to image both shallower structure and deeper structure.

Some methods also seek to recover (usually, mantle) anisotropy.

The joint inversion of RFs and SWs has become a standard seismological technique.

Many current studies seek to fit additional datasets like travel times and attenuation/blockage.

Results are being integrated across wider regions for tectonic interpretation.